NANO LETTERS

pubs.acs.org/NanoLett

Extended Mapping and Exploration of the Vanadium Dioxide Stress-Temperature Phase Diagram

J. Cao,[†,§] Y. Gu,[¶] W. Fan,[†,#] L. Q. Chen,[¶] D. F. Ogletree,[§,∥] K. Chen,[⊥] N. Tamura,[⊥] M. Kunz,[⊥] C. Barrett,[†,§] J. Seidel,[‡,§] and J. Wu*[,†,§]

[†]Department of Materials Science and Engineering and [‡]Department of Physics, University of California, Berkeley, California 94720, [§]Materials Sciences Division, [∥]Molecular Foundry, and [⊥]Advanced Light Source, Lawrence Berkeley National Laboratory, Berkeley, California 94720, [¶]Department of Materials Science and Engineering, Penn State University, University Park, Pennsylvania 16802, and [#]Department of Thermal Science and Energy Engineering, University of Science and Technology of China, Hefei, China

ABSTRACT Single-crystal micro- and nanomaterials often exhibit higher yield strength than their bulk counterparts. This enhancement is widely recognized in structural materials but is rarely exploited to probe fundamental physics of electronic materials. Vanadium dioxide exhibits coupled electronic and structural phase transitions that involve different structures existing at different strain states. Full understanding of the driving mechanism of these coupled transitions necessitates concurrent structural and electrical measurements over a wide phase space. Taking advantages of the superior mechanical property of micro/nanocrystals of VO_2, we map and explore its stress-temperature phase diagram over a phase space that is more than an order of magnitude broader than previously attained. New structural and electronic aspects were observed crossing phase boundaries at high-strain states. Our work shows that the actively tuning strain in micro/nanoscale electronic materials provides an effective route to investigate their fundamental properties beyond what can be accessed in their bulk counterpart.

KEYWORDS Strain, phase transition, correlated electron nanomaterials, vanacium dioxide, mechanical strength

Strongly correlated electron materials develop many of their remarkable physical properties from the interplay between spin, charge, and lattice degrees of freedom.[1] The delicate cross-coupling makes these properties sensitive to a variety of chemical and physical stimuli. Lattice strain is one of these stimuli, which has been used to enhance order parameters in ferroelectric[2,3] and high-critical temperature superconducting thin films.[4] Vanadium dioxide (VO_2) is a strongly correlated electron material that exhibits a metal−insulator transition (MIT) coupled with a rutile (R)−monoclinic (M1) structural transition.[5,6] It is known that the transition temperature and domain structure are profoundly affected by uniaxial strains.[7−10] The MIT can be further complicated at large strain or high Cr doping that induces another monoclinic structure of VO_2, the M2 phase.[5,11−15] In epitaxial thin films, biaxial strain results from lattice mismatch with the underlying substrate, and hence the amount of strain that can be imposed on the film depends on the availability of isostructural substrates with different lattice parameters.[16] Furthermore, the strain in the film can be redistributed by possible presence of misfit dislocations and grain boundaries, which typically result in microscopic domain structures that limit the phase space accessible in experiments and complicate the interpretation of results.[17,18] Free-standing, single-crystal nanomaterials, on the other hand, can be subjected to uniform and continuously tunable uniaxial strain. The lack of structural defects in these materials allow them to withstand much higher strain (>2%) than their bulk counterpart (<0.2%) without fracturing,[9] enabling in situ investigations at the single domain level of strain states that are otherwise inaccessible. Research in nanostructured VO_2, for example, has recently shed new light on the properties of the elusive M2 phase.[12−15] The electronic nature of the transitions between the M1, M2, and R structural phases, however, has not been elucidated across the broad phase space. Combining in situ microscopic imaging and micro X-ray diffraction (μXRD) on single domains of crystalline VO_2 microbeams, we have mapped its complicated phase diagram over a range of strain that is more than an order of magnitude broader than previously attained. Electronic phase transitions among the three structures were activated by assembling microbeams into devices where high tensile or compressive stress could be applied. New structural and electronic aspects were observed for phase transitions at high-strain states. Under tensile strain the M2 phase self-organizes into twinned superlattices and can be transformed reversibly to the R or M1 phases by varying temperature or stress. The resistivity of the M2 phase is three times higher than the M1 phase. Our work shows that actively tuning strain in crystalline-correlated electron

* To whom correspondence should be addressed. E-mail: wuj@berkeley.edu.
Received for review: 04/25/2010
Published on Web: 06/29/2010

DOI: 10.1021/nl101457k | *Nano Lett.* **2010,** *10,* 2667–2673

micro/nanomaterials provides an effective means to extensively modulate electronic phases and reveal emergent properties.

In the strain-free state, VO_2 undergoes a first-order MIT with a drastic change in electronic and optical properties at $T_C^0 = 341$ K.[5,6,19] The MIT is accompanied with the structural change from the high-temperature, tetragonal, metallic phase (rutile structure, R) to the low-temperature, monoclinic, insulating phase (M1). The latter structure is characterized by a dimerization of vanadium atoms and a tilt of these pairs with respect to the R-phase c axis (c_R).[5] It has been a topic of debate[5,20] for decades whether the MIT is fundamentally a Mott transition driven by electron−electron correlation, or a Peierls transition driven by electron−lattice interactions. It is known that the monoclinic M2 structure can be induced by doping with Cr or uniaxial compression perpendicular to c_R.[5,6,11] In the M2 phase, only half of the vanadium atoms dimerize while the other half form zigzag chains. Because of the difficulty of accessing the undoped M2 phase, its role in the MIT and its electrical properties have not been clearly established.[5] The free energy of M2 in undoped VO_2 is believed to be very close to that of M1 around T_C^0, making it difficult to stabilize a pure M2 phase.[11]

Vanadium dimerization leads to a unit cell doubling in the monoclinic M1 and M2 structures relative to the R structure. The structural transition from M1 to R effectively shrinks the specimen along the c_R direction by $\varepsilon_0 \approx 1\%$, while the transition from M1 to M2 expands it along c_R by $\varepsilon_0 \approx 0.3\%$.[6] We note that a triclinic phase (T) might also derive from the M1 structure, but only with a continuous change in lattice constant and angles.[5,6] Detailed lattice parameters of the M1, M2, and R structures are summarized in the Supporting Information. Uniaxial compression (tension) along c_R direction tends to drive the M1 phase toward the R (M2) phase. The critical stress needed to trigger a transition at temperature T_C is given by the uniaxial Clapeyron equation

$$\frac{d\sigma_c}{dT_c} = \frac{\Delta H}{\varepsilon_0 T_c^0} \quad (1)$$

where ΔH is the latent heat of the transition.

During vapor-transport synthesis,[21] single-crystal VO_2 micro- and nanobeams grow along the c_R direction at high temperatures (~1200 K) on a molten SiO_2 film on a Si wafer. When cooled to lower temperatures, the SiO_2 surface solidifies leaving some VO_2 microbeams free-standing and some bottom clamped onto the SiO_2 surface.[7] In the latter case, because of the thermal expansion mismatch between SiO_2 and VO_2 combined with the c_R change across the MIT, the VO_2 beams are clamped in different strain states varying from beam to beam depending on local conditions during the cooling process (Supporting Information Figure S2). The free-standing beams show an abrupt single jump in both optical reflectivity and electrical resistivity at T_C, while the bottom-clamped beams show metal−insulator domains self-organized along the beam length.[7,9] High-resolution scanning electron microscopy (SEM) images of these two types of beams revealed new information, as shown in Figure 1a,b. The free-standing beams always have a smooth, featureless surface that does not change as temperature increases. The bottom clamped beams, however, often show periodic stripes parallel to the c_R direction with a period of ~150 nm. At room temperature these stripes span the entire length of the beam. With increasing temperature, new domains with a smooth surface nucleate out of the striped phase and eventually grow and eliminate the stripes at high temperatures. Using atomic force microscopy (AFM), we found that a weak surface corrugation is associated with the striped contrast in the SEM images. Figure 1c shows the morphology of the beam surface obtained at 333 K using AFM. The surface corrugation has an amplitude of ~0.7 nm, corresponding to a corrugation angle of ~0.6°.

It has been established that under white-light illumination, the insulating phase of VO_2 shows a brighter optical reflectivity than the metallic (R) one.[7] Comparing Figure 1 panels a and b with optical images of the beams (Supporting Information Figure S3), it is clear that (i) the metallic R phase always has no surface corrugation, (ii) the insulating phase has no corrugation for free-standing beams, and (iii) bottom clamping can cause surface corrugation in the insulating phase. In a previous work, we demonstrated that in-plane bending of VO_2 microbeams generated self-organized triangular metal−insulator domains so as to maximally relax the strain energy.[9] Figure 1d shows an optical image of these domains at T_C^0 together with a close-up SEM image of one of the triangular insulator domains. It can be seen that the striped phase is insulating and stabilized by tensile strain. In the following, we identify the striped phase to be a twinned M2 structure, map the M1−M2−R phase diagram over an unprecedentedly wide phase space, and measure the changes in electronic properties between these phases.

We used μXRD to elucidate the crystal structure of the submicrometer sized domains along the VO_2 microbeams. For free-standing beams with no surface corrugation, the μXRD Laue pattern shows the M1 structure at $T < T_C^0$ and the R structure at $T > T_C^0$ as expected with the beam length along the a_{M1}/c_R axis, and $\{011\}_{M1}/\{110\}_R$ planes as the bounding faces (Supporting Information Figures S4 and S5). For the bottom-clamped beams that show the striped phase, however, a splitting of the μXRD spots was observed in the Laue pattern, as shown in Figure 2a. The VO_2 spots were indexed to the M2 structure with two polysynthetic twins labeled as M2α and M2β as shown in Figure 2b. These twinned components have $(201)_{M2}$ and $(\bar{2}01)_{M2}$ planes as the top surface, respectively, which will both transform into the $(110)_R$ plane upon the MIT. The two M2 components have b_{M2} and a_{M2} axes rotated 180° with respect to each other, and c_{M2} becomes a 2-fold symmetry axis with respect to the

DOI: 10.1021/nl101457k | Nano Lett. 2010, 10, 2667--2673

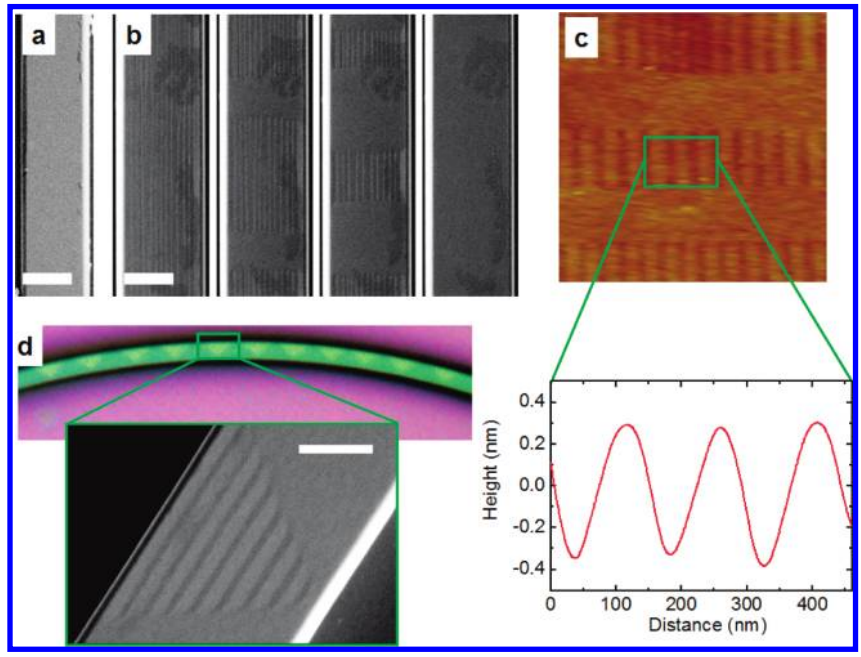

FIGURE 1. Striped phase of tensile strained VO_2 microbeams. (a) Top-view high-resolution SEM image of a free-standing VO_2 beam at 298 K showing a featureless surface. No change was observed at elevated temperatures. (b) SEM images of a bottom-clamped VO_2 beam at 298, 323, 333, and 368 K (left to right), showing progressive reduction of the striped phase with increasing temperature. (c) AFM image of the clamped VO_2 beam at 333 K, showing periodic surface corrugation of the striped phase. (d) High-resolution optical and SEM images of a bent VO_2 beam near the natural metal−insulator transition temperature (341 K), showing an array of triangular insulating (bright) and metallic (dark) domains and fine striped structure within insulating domains. The scale bar is 1 μm in a and b and 500 nm in d.

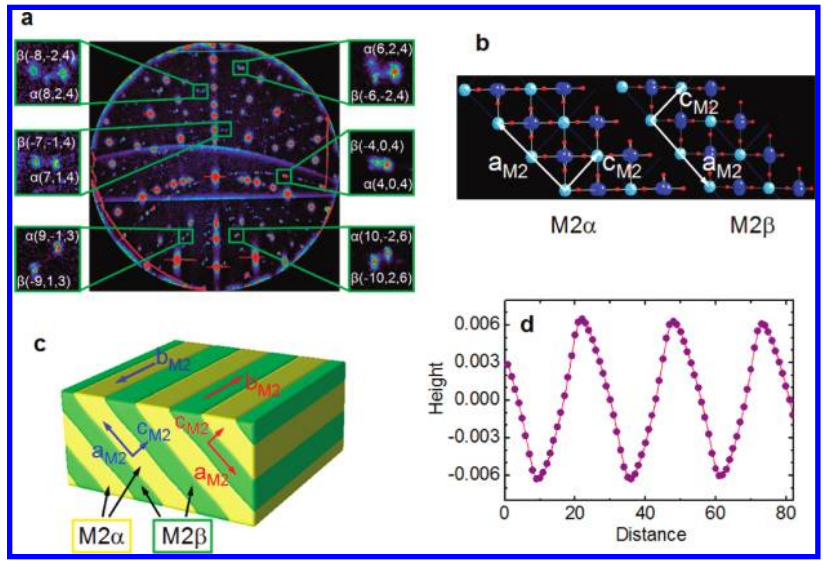

FIGURE 2. Twinned M2 structure in axially strained VO_2 beams. (a) Typical room-temperature μXRD pattern of a bottom-clamed VO_2 beam indexed as a twinned monoclinic M2 phase (M2α/M2β). The brightest spots come from the Si substrate, while the remaining ones showing splitting are from the VO_2 beam. (b) Crystal structure viewed along the beam growth direction (b_{M2} or c_R) showing the epitaxially jointed $(001)_{M2}$ planes as the twin interface. The small red dots represent oxygen, and the blue and cyan dots represent two types of vanadium atoms in the M2 structure. The angle between a_{M2} and c_{M2} is 91.2°. (c) Phase-field simulation of strained VO_2 showing the polysynthetic twinning of the M2 phase with $(001)_{M2}$ as the composition interface. Green and yellow colors represent the two types of M2 variants, M2α and M2β. (d) Surface corrugation profile calculated by phase field simulations. The units are grids, which are assigned to 10 nm in the simulations.

twinning variants (Figure 2c). This configuration resembles the structures observed in polysynthetic twins in ferroelectric Rochelle salts[22,23] and twinning superlattices recently found in doped InP nanowires.[24] Our experiments also agree with the recent reports of Raman observation of M2 structure and dimensions of the stripped phase.[15]

Theoretically, the M2 structure has four variants with different transformation strain tensors, where each two of

DOI: 10.1021/nl101457k | *Nano Lett.* **2010,** *10,* 2667--2673

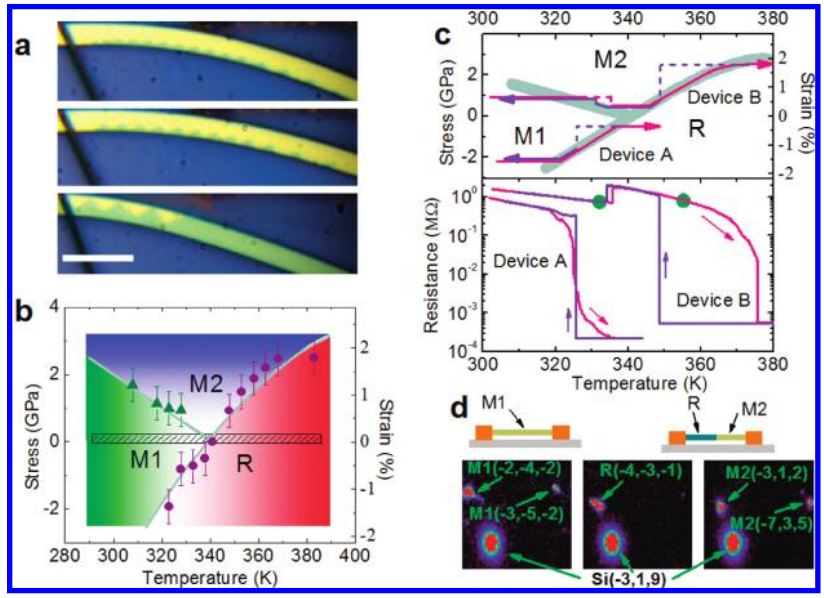

FIGURE 3. Mapping and exploring the broad phase diagram of VO_2. (a) Optical images of bending a cantilevered VO_2 microbeam at 328, 333, and 363 K (top to down). The bending displacement in each case is slightly above the threshold so as to better show the domains of the new phase (insulating or metallic). Scale bar is 10 μm. (b) The uniaxial stress (along c_R)−temperature phase diagram of VO_2 obtained by in situ optical and SEM imaging of VO_2 beam bending. The lines are guides to the eyes. The hatched rectangular area near zero strain is the narrow phase space previously explored in bulk VO_2.[11] The error bars are from measuring multiple samples. (c) Temperature-dependent resistance of a device on bendable substrate (Device A) and an end-end clamped device (Device B). The upper panel shows their traces on the phase diagram during the heating−cooling cycle. The dashed parts of the traces represent superheating/supercooling. (d) Schematic views of the microbeam in Device B in the pure M1 state obtained at 333 K (left) and in the M2−R coexisting state obtained at 353 K (middle and right) during heating, and representative μXRD pattern at the same reciprocal-space location. The middle and right μXRD patterns were recorded from two different positions along the microbeam. These two temperatures are labeled with green dots on the curve in the lower panel of c.

them can be combined to form one kind of twins. Among these possible combinations, only two of them have 2-fold rotational symmetry with respect to c_{M2} axis (Supporting Information). Marezio et al. also predicted and experimentally observed four twin laws for the M2 phase in VO_2 induced by Cr doping,[25] that is, $(\bar{2}01)_{M2}$, $(201)_{M2}$, $(100)_{M2}$, and $(001)_{M2}$. Following Khchaturyan's domain structure analysis to minimize the heterogeneous strain energy,[26] we obtained the same twin habit orientation for the two c_{M2} variants as in Figure 2b. We used a three-dimensional (3D) phase field model to simulate the domain structure of the M2 phase. The modeling results reveal two degenerate polysynthetic twinning states with $(100)_{M2}$ or $(001)_{M2}$ as the domain boundary. Figure 2c shows the simulated domain structure of the $(001)_{M2}$ twinning habit, where the two variants M2α and M2β form alternating thin platelets that rotate 45° to the left side from the vertical direction. The $(100)_{M2}$ twinning has the same configuration except that the twinning variants rotate 45° to the right side. Both degenerate twinning habits will result in stripes parallel to b_{M2} (or c_R) direction on the top surface, agreeing with the experimental observation. The tilting of the M2α and M2β variants at the cross section is verified by the observation of kinked stripes near the edge of a VO_2 microbeam imaged in normal direction (Supporting Information Figure S6). As shown in Figure 2d, the calculated surface corrugation resulted from the alternating variants agrees qualitatively with experimental data (Figure 1c). We also simulated possible combinations of the other two M2 variants, that is, the twinning with composition interface of $(\bar{2}01)_{M2}$ or $(201)_{M2}$. However, their domain structures do not form regularly aligned stripes due to a small magnitude of transformation strain for these variant combinations. For the R to M1 transition, the transformation strain is much smaller than the R to M2 transition (Supporting Information), and hence an applied stress has a greater effect on the stability of the M2 phase than the M1 phase.

To experimentally quantify the boundaries between these phases, we differentiate the insulating M1/M2 phases from the metallic R phase by their different optical contrast, and the M1 phase from M2 phase by the surface corrugation in the latter. We prepared VO_2 microbeams with one end clamped and the rest free on a SiO_2 substrate; using a microprobe tip, the beam was bent horizontally on the substrate and simultaneously subject to high-resolution optical or SEM imaging at various temperatures. The root of the beam close to the anchoring point bears the highest compressive or tensile stress at the concave or convex edge, respectively. At various temperatures, the beam was bent until the first domain was seen to nucleate out of the original phase; the bending displacement of the beam was then used to calculate the critical strain and stress at that temperature, which defines the phase boundary. Figure 3a shows optical images of a VO_2 beam bent slightly beyond the critical

DOI: 10.1021/nl101457k | *Nano Lett.* **2010,** *10,* 2667--2673

curvature at 328, 333, and 363 K. It is clearly seen that a larger curvature is needed to trigger the MIT at temperatures farther away from T_C^0, either above or below. Similar experiments were performed inside a SEM where the emergence of the striped M2 phase similar to that in the inset of Figure 1d signifies the critical tensile stress needed to cross the M1−M2 boundary. The boundaries obtained in this way are plotted in Figure 3b and define the stress-temperature phase diagram of VO_2. Note that most of the samples investigated are beams wider than 500 nm, so we do not expect any size effect.

The slope of the insulating (M1 or M2)−R boundary determines the latent heat of the transitions through eq 1. The phase boundaries are approximately linear near the triple point while they deviate from the straight line at large strains. Fitting the linear part of the experimental data we obtain a latent heat of $\Delta H = 1200 \pm 200$ Cal/mol (or 5.0 ± 0.8 kJ/mol), which is consistent with literature data of 1025 Cal/mol.[27,28] Because of the limited uniaxial strain attainable in the bulk (<0.2%) and lack of substrates to stabilize uniform epitaxial strain, the stress-temperature phase diagram of VO_2 has been previously established only within a narrow tensile region near the triple point around T_C^0, as shown in Figure 3b.[11] The superior mechanical flexibility of the VO_2 microbeams allows us to map the phase diagram over a phase space that is more than an order of magnitude broader. A latent heat of $\Delta H = 200 \pm 40$ Cal/mol (or 0.84 ± 0.17 kJ/mol) was estimated from Figure 3b for the M1−M2 transition. This value is also in good agreement with previous reported values of $\Delta H = 230 \pm 40$ Cal/mol[29] or 205 ± 40 Cal/mol[11] measured from bulk VO_2 in close proximity of T_C^0. Note that the stress was applied along the $[110]_R$ direction in previous work,[11] while it was along the $[001]_R$ direction in our work. Both the slope $d\sigma_c/dT_c$ and spontaneous strain across the transition (ε_0) are different in these two cases. The Clapeyron equation gives rise to the same latent heat as expected. However, the latent heat in this work was determined over a much wider strain range than in ref 11. This is consistent with that fact that the boundary lines between M1, M2, and R are approximately linear in this strain range (∼1%). The nonlinearity of the phase boundary at higher strains (>∼1%) may provide new insight of the phase transition and warrants further investigation.

For the M2 phase induced by Cr doping, the resistivity has been reported to be 25% higher than the neighboring M1 phase.[30] The fact the M2 phase is still insulating in spite of its undimerized vanadium chains has been used to argue that the MIT in VO_2 is electronically driven.[31] To directly compare the electrical conductivity of all undoped M1, M2, and R phases, we fabricated VO_2 devices and examined the transitions among these phases. Two types of devices were fabricated, (A) devices on bendable substrates to explore the compressive phase space where a direct M1−R transition is expected; and (B) end−end-clamped devices made from as-grown microbeams to explore the tensile phase space where an M1−M2−R transition is expected. Type A devices were fabricated and clamped on a plastic substrate and compressive strain was induced by controlling the substrate bending curvature.[32] For type B devices, as-grown, bottom-clamped VO_2 microbeams were etched into an end−end-clamped configuration following Wei et al.[8] Because of the restriction of constant length in type B devices, a uniform stress exists along the beam length and supports coexistence of two phases; in its equilibrium state the system is constrained to move along the phase boundary,[18] akin to isochoric process in liquid−vapor phase transitions.[33]

The temperature-dependent resistance of representative devices of types A and B are shown in Figure 3c. For Device A, the resistance starts to deviate from the insulating-phase Arrhenius dependence at 320 K < T_C^0 as it continuously enters the M1−R coexisting state. At 335 K, the resistance reaches a stable, metallic value, 3 orders of magnitude lower than that of the M1 phase. Upon cooling, the device stays in the R state until 325 K, where it makes a discontinuous jump from the supercooled, metastable R state to the M1−R coexisting state. For Device B, the resistance shows an upward jump at $T_1' = 334$ K, and then gradually decreases until $T_2 = 372$ K where it drops to the metallic value. Upon cooling, the resistance jumps upward at $T_2' = 348$ K, and afterward it approximately follows the trajectory of the heating process, first increasing and then jumping down to the original resistance.

To identify the structure along these electronic phase transitions, we carried out μXRD experiments at various positions along the microbeam of Device B at selected temperatures. A pure M1 structure was seen between room temperature and T_1'. Between 345 K and T_2, the M2 structure was observed on one part and the R structure on the other part of the microbeam, directly demonstrating the coexistence of M2 and R phases within this temperature range. Above T_2, a single R phase was observed along the entire microbeam. On the basis of this information, the process trajectory is traced on the phase diagram in the top panel in Figure 3c. It can be seen that the microbeam starts in M1 phase in a tensile-strained state estimated to be $\varepsilon_1 \sim 0.7\%$, insufficient to induce M2 phase. As temperature is increased to $T_1 \approx 325$ K, the trace crosses the M1-M2 boundary but the microbeam stays in the superheated M1 phase. At T_1' the penalty in free energy of staying in M1 is higher than the nucleation energy barrier of M2, such that the system switches into the M2 phase, and the total strain is reduced to $\varepsilon_1 - 0.3\% = 0.4\%$. The resistance jump at T_1' of a factor of 3 indicates that the M2 phase is three times as resistive as the M1 phase at those strain states. At $T \approx 345$ K, the system reaches the M2−R boundary and moves along it until T_2 where it enters the pure R phase with a strain of $\varepsilon_1 + 1\% = 1.7\%$. Upon cooling the system retraces this trajectory except for the supercooling effect at the R−M2 and M2−M1 boundaries. It is intriguing to note the different supersaturation behavior along the phase transitions; large

DOI: 10.1021/nl101457k | Nano Lett. 2010, 10, 2667--2673

supercooling was seen on the transitions involving the MIT (i.e., M1−R and M2−R), but not on the structural transition (M1−M2). This distinction suggests that the nucleation energy barrier through the MIT of VO_2 is primarily electronic, supporting the fundamental role of electron correlation in the MIT. The electronic phase transitions among these three structures are therefore achieved at both high compressive and tensile conditions far beyond previously explored phase space and show behavior consistent with the phase diagram mapped out by μXRD.

In summary, we mapped the uniaxial stress−temperature phase diagram of VO_2 over an order of magnitude wider strain range than previously achieved. This was enabled by the superior mechanical properties of single-crystal microbeams that supported extraordinarily high strains to induce structural and electronic phase transitions. We also stabilized the pure M2 phase in undoped VO_2 and observed twinning at the submicrometer scale. These phase transitions were characterized by a combination of optical, electron, and atomic force microscopies and micro-X-ray diffraction, and analyzed through 3D phase-field modeling. Electrical resistance across the insulating M1 and M2 and metallic R phases was measured over the extended phase diagram, and the M2 resistivity was found to be three times greater than M1. Our approach can be applied to other strongly correlated electron materials to map phase space as well as reveal and engineer new properties.

Methods. Single-crystalline VO_2 microbeams were grown using the vapor transport method reported previously[7,21] and characterized using μXRD and SEM. Laue diffraction was performed using the synchrotron white X-ray beam at the Beamline 12.3.2 in the Advanced Light Source (ALS) at the Lawrence Berkeley National Laboratory. Diffraction data were collected in reflection mode using a large-area charge coupled device detector (MAR 133). The diffraction patterns were analyzed and indexed using the XMAS software developed at the ALS. Experimental geometrical parameters such as the sample−detector distance, center channel position, and detector tilt were calibrated using the Si substrate spots as reference. The focused X-ray spot was <1 μm and was aligned to the VO_2 microbeam by X-ray fluorescence collected from vanadium atoms using a VORTEX Si-drift detector.

A percentage of VO_2 microbeams were grown with one-end anchored on the SiO_2 substrate during the synthesis and naturally formed side-bending cantilevers. In situ optical experiments were carried out on a CASCADE Microtech M150 probe station equipped with a high resolution optical microscope. In situ SEM experiments were performed in a Zeiss Gemini Supra 55 VP-SEM equipped with a Kleindiek MM3A nanomanipulator and a Peltier stage and a thermocouple for temperature control. The critical stress was calculated using the cantilever bending equation $\sigma = 3wtY/a^2$, where w is the bending displacement, t is half of the beam width, $Y = 140$ GPa[34] is the beam Young's modulus of the M1 phase, and a is the distance between the force location and the anchor point on the beam.

To fabricate type A devices, a single-crystal VO_2 beam was transferred to a Cirlex Kapton substrate (thickness ~1 mm), and subsequently metal electrodes (15 nm Cr and 400 nm Au) were patterned using standard lithography and deposited using sputtering. Epoxy was used to embed and bind the VO_2 beam onto the substrate and cured immediately at 390 K for 30 min. This step assured that the VO_2 beam was clamped while in the R phase and induced a compressive strain of ~1.4% (1% due to the MIT and 0.4% due to thermal expansion mismatch between VO_2 and the plastic substrate) when cooled down to room temperature. Type B devices were fabricated following Wei et al.,[8] in which metal electrodes were patterned and deposited on as-grown, bottom-clamped VO_2 microbeams, and subsequently the uncovered SiO_2 was etched away using buffered oxide etchant, so as to liberate the VO_2 beam into an end−end-clamping configuration. No mechanical buckling/unbuckling along the beam was observed by SEM in the experimental temperature range. Here we assumed an initial strain value in Device B and compared its resistance-temperature curve and μXRD data with the phase diagram independently mapped out by the in situ SEM, by which we determined the best-fit initial strain in Device B.

In the phase-field simulation, we used two order parameters, η_1 and η_2, for the two M2 variants. The total energy of the system consists of bulk free energy and the elastic strain energy

$$F(\eta_1, \eta_2) = \sum_{n=1,2} [f(\eta_n) + \frac{1}{2} C_{ijkl}(\varepsilon_{ij} - \eta_n^2 \varepsilon_{ij}^0)(\varepsilon_{kl} - \eta_n^2 \varepsilon_{kl}^0)]$$

The system is constrained by a substrate at the bottom, a thin film layer (0.6 μm) in the middle, and a gas phase on the top. Thin film boundary conditions (clamped on both the length and width directions by a preset mismatch strain) were employed. An iteration method developed for inhomogeneous system[35] was used to obtain the elastic solution.

Acknowledgment. This work was supported by the Laboratory Directed Research and Development Program of Lawrence Berkeley National Laboratory (LBNL) under U.S. Department of Energy Contract No. DE-AC02-05CH11231 [Dr. J. Cao and measurements], by the National Science Foundation (NSF) under Grant EEC-0832819 [material synthesis and device fabrication], and NSF DMR-0507146 [theory and modeling]. Portions of this work were performed as user projects at the Molecular Foundry [in situ SEM] and at the Advanced Light Source [μXRD], LBNL, which is supported by the Office of Science, Office of Basic Energy Sciences, of the U.S. Department of Energy under Contract No. DE-AC02-05CH11231. We thank Dr. E. Saiz and Dr. M. Raschke for useful discussions.

DOI: 10.1021/nl101457k | *Nano Lett.* **2010,** *10,* 2667--2673

Supporting Information Available. Details of the phase field modeling, Tables S1 and S2, Figures S1−S6, and additional references. This material is available free of charge via the Internet at http://pubs.acs.org.

REFERENCES AND NOTES

(1) Spaldin, N. A.; Fiebig, M. *Science* **2005**, *309*, 391–392.
(2) Haeni, J. H.; Irvin, P.; Chang, W.; Uecker, R.; Reiche, P.; Li, Y. L.; Choudhury, S.; Tian, W.; Hawley, M. E.; Craigo, B.; Tagantsev, A. K.; Pan, X. Q.; Streiffer, S. K.; Chen, L. Q.; Kirchoefer, S. W.; Levy, J.; Schlom, D. G. *Nature* **2004**, *430*, 758–761.
(3) Choi, K. J.; Biegalski, M.; Li, Y. L.; Sharan, A.; Schubert, J.; Uecker, R.; Reiche, P.; Chen, Y. B.; Pan, X. Q.; Gopalan, V.; Chen, L.-Q.; Schlom, D. G.; Eom, C. B. *Science* **2004**, *306*, 1005–1009.
(4) Locquet, J. P.; Perret, J.; Fompeyrine, J.; Maechler, E.; SEO, J. W.; van Tendeloo, G. *Nature* **1998**, *394*, 453–456.
(5) Eyert, V. *Ann. Phys. (Berlin)* **2002**, *11* (9), 650–704.
(6) Marezio, M.; McWhan, B.; Dernier, P. D.; Remeika, J. P. *Phys. Rev. B* **1972**, *5* (7), 2541–2551.
(7) Wu, J.; Gu, Q.; Guiton, B. S.; de Leon, N.; Lian, O.; Park, H. *Nano Lett.* **2006**, *6*, 2313–2317.
(8) Wei, J.; Wang, Z.; Chen, W.; Cobden, D. H. *Nat. Nanotechnol.* **2009**, *4*, 420–424.
(9) Cao, J.; Ertekin, E.; Srinivasan, V.; Fan, W.; Huang, S.; Zheng, H.; Yim, J. W. L.; Khanal, D. R.; Ogletree, D. F.; Grossman, J. C.; Wu, J. *Nat. Nanotechnol.* **2009**, *4*, 732–737.
(10) Tselev, A.; Strelcov, E.; Luk'yanchuk, I. A.; Budai, J. D.; Tischler, J. Z.; Ivanov, I. N.; Jones, K.; Proksch, R.; Kalinin, S. V.; Kolmakov, A. *Nano Lett.* , *10* (6), 2003–2011.
(11) Pouget, J. P.; Launois, H.; D'Haenens, J. P.; Merenda, P.; Rice, T. M. *Phys. Rev. Lett.* **1975**, *35*, 873–875.
(12) Sohn, J. I.; Joo, H. J.; Ahn, D.; Lee, H. H.; Porter, A. E.; Kim, K.; Kang, D. J.; Welland, M. E. *Nano Lett.* **2009**, *9*, 3392–3397.
(13) Zhang, S.; Chou, J. Y.; Lauhon, L. J. *Nano Lett.* **2009**, *9*, 4527–4532.
(14) Booth, J. M.; Casey, P. S. *ACS Appl. Mater. Interfaces* **2009**, *1*, 1899–1905.
(15) Jones, A.; Berweger, S.; Wei, J.; Cobden, D. H.; Raschke, M. *Nano Lett.* **2010**, *10*, 1574–1581.
(16) Schlom, D. G.; Chen, L. Q.; Eom, C. B.; Rabe, K. M.; Streiffer, S. K.; Triscone, J. M. *Annu. Rev. Mater. Res.* **2007**, *37*, 589–626.
(17) Qazilbash, M. M.; Brehm, M.; Chae, B. G.; Ho, P. C.; Andreev, G. O.; Kim, B. J.; Yun, S. J.; Balatsky, A. V.; Maple, M. B.; Keilmann, F.; Kim, H. T.; Basov, D. N. *Science* **2007**, *318*, 1750–1753.
(18) Natelson, D. *Nat. Nanotechnol.* **2009**, *4*, 406–407.
(19) Rakotoniaina, J. C.; Mokranitamellin, R.; Gavarri, J. R.; Vacquier, G.; Casalot, A.; Calvarin, G. *J. Solid State Chem.* **1993**, *103* (1), 81–94.
(20) Wentzcovitch, R. M.; Schultz, W. W.; Allen, P. B. *Phys. Rev. Lett.* **1994**, *72* (21), 3389–3392.
(21) Guiton, B. S.; Gu, Q.; Prieto, A. L.; Gudiksen, M. S.; Park, H. *J. Am. Chem. Soc.* **2005**, *127*, 498–499.
(22) Mitsui, T.; Furuichi, J. *Phys. Rev.* **1953**, *90*, 193.
(23) Klassen-Neklyudova, M. V. *Mechanical Twinning of Crystals*; Consultants Bureau: New York, 1964.
(24) Algra, R. E.; Verheijen, M. A.; Borgstroem, M. T.; Feiner, L. F.; Immink, G.; van Enckevort, W. J. P.; Vlieg, E.; Bakkers, E. P. A. M. *Nature* **2008**, *456*, 369–372.
(25) Marezio, M.; Dernier, P. D.; Santoro, A. *Acta Crystallogr, Sect. A* **1973**, *29*, 618–621.
(26) Khachaturyan, A. G. *Theory of Structural Transformations in Solids*; Dover Publications: Mineola, NY, 2008.
(27) Cook, O. A. *J. Am. Chem. Soc.* **1964**, *69*, 331–333.
(28) Berglund, C. N.; Guggenheim, H. J. *Phys. Rev.* **1969**, *185*, 1022–1033.
(29) Pouget, J. P.; Launois, H.; Rice, T. M.; Dernier, P.; Gossard, A.; Villeneu, G.; Hagenmul, P. *Phys. Rev. B* **1974**, *10* (5), 1801–1815.
(30) Zylbersztejn, A.; Mott, N. F. *Phys. Rev. B* **1975**, *11* (11), 4383–4395.
(31) Rice, T. M.; Launois, H.; Pouget, J. P. *Phys. Rev. Lett.* **1994**, *73*, 3042.
(32) Yang, R.; Qin, Y.; Dai, L.; Wang, Z. L. *Nat. Nanotechnol.* **2009**, *4*, 34–39.
(33) McQuarrie, D. A.; Simon, J. D. *Physical Chemistry: A Molecular Approach*; University Science Books: Sausalito, CA, 1997.
(34) Tsai, K. Y.; Chin, T. S.; Shieh, H. P. D. *Jpn. J. Appl. Phys.* **2004**, *43* (9A), 6268–6273.
(35) Hu, S. Y.; Chen, L. Q. *Acta Mater.* **2001**, *49*, 1879–1890.

DOI: 10.1021/nl101457k | *Nano Lett.* **2010,** *10,* 2667--2673

Extended Mapping and Exploration of the Vanadium Dioxide Stress-Temperature Phase Diagram

J. Cao[1, 2] , Y. Gu[3], W. Fan[1, 4], L. Q. Chen[3], D. F. Ogletree[2,5], K. Chen[6], N. Tamura[6], M. Kunz[6], C. Barrett [1, 2], J. Seidel [2,7], and J. Wu[1, 2, *]

[1]Department of Materials Science and Engineering, University of California, Berkeley, CA 94720, USA

[2]Materials Sciences Division, Lawrence Berkeley National Laboratory, Berkeley, CA 94720, USA

[3]Department of Materials Science and Engineering, Penn State University, University Park, PA, 16802, USA

[4]Department of Thermal Science and Energy Engineering, University of Science and Technology of China, Hefei, China

[5]Molecular Foundry, Lawrence Berkeley National Laboratory, Berkeley, CA 94720, USA

[6]Advanced Light Source, Lawrence Berkeley National Laboratory, Berkeley, CA 94720, USA

[7]Department of Physics, University of California, Berkeley, CA 94720, USA

*To whom correspondence should be addressed. Email: wuj@berkeley.edu

This file includes:

Table S1 Possible Twins for the M2 structure

Table S2 Lattice parameters of the R, M1, and M2 structures

Figure S1 Side-viewed structure of VO_2 in the M1, R, and M2 phases

Figure S2 Schematic plot of unstrained effective lattice constant (c) along c_R direction as a function of temperature

Figure S3 Bright-field reflected optical images of a bottom-clamped VO_2 beam under white-light illumination

Figure S4 Laue diffraction pattern of a free-standing VO_2 beam at 298K (M1 phase)

Figure S5 Laue diffraction pattern of a free-standing VO_2 beam at 360 K (R phase)

Figure S6 Apparently kinked M2 stripes at the edge of a bottom-clamped VO_2 beam viewed from the perpendicular direction, indicating the tilting of the M2α and M2β domains away from the perpendicular direction in the cross section of the beam.

Phase field modeling and twin structure analysis

To understand the domain pattern in VO_2, we used a three-dimensional phase field model to simulate the formation of domains in M2 phases. The R to M2 transition has four variants with different transformation strain tensors as shown below,

$$\varepsilon_1=\begin{pmatrix}\varepsilon_{11} & \varepsilon_{12} & 0\\ \varepsilon_{12} & \varepsilon_{22} & 0\\ 0 & 0 & \varepsilon_{33}\end{pmatrix},\varepsilon_2=\begin{pmatrix}\varepsilon_{11} & -\varepsilon_{12} & 0\\ -\varepsilon_{12} & \varepsilon_{22} & 0\\ 0 & 0 & \varepsilon_{33}\end{pmatrix},\varepsilon_3=\begin{pmatrix}\varepsilon_{22} & \varepsilon_{12} & 0\\ \varepsilon_{12} & \varepsilon_{11} & 0\\ 0 & 0 & \varepsilon_{33}\end{pmatrix},\varepsilon_4=\begin{pmatrix}\varepsilon_{22} & -\varepsilon_{12} & 0\\ -\varepsilon_{12} & \varepsilon_{11} & 0\\ 0 & 0 & \varepsilon_{33}\end{pmatrix},$$

where $\varepsilon_{11}=-0.0038728,\varepsilon_{22}=-0.00383993,\varepsilon_{33}=0.0176978,\varepsilon_{12}=-0.0164594$. These variants can be combined to form different twinning structures. It is noticed that only the combinations of variant 1 & 2 and variant 3 & 4 are two-fold rotationally symmetric with respect to c_{M2}. Following Khachaturyan's domain structure analysis[1], the possible combinations are summarized in Table S1. In case I, variant 1&2 or 3&4 can be combined together to form polysynthetic twinning structures with twin habit normal of $(100)_{M2}$ or $(001)_{M2}$. In case II, the twin habit normal becomes $(\bar{2}01)_{M2}$ or $(201)_{M2}$. However, phase field simulations shows that these latter domain structures do not exhibit any preferred orientation with respect to each other. This may be caused by their very small strain. Case III and IV provides numerically the same results as case I.

Table S1 Possible Twins for the M2 structure

Possible combination	Heterogeneous stress-free transformation strain $\Delta\varepsilon^0$	Twin habit normal	ε^0 (magnitude of $\Delta\varepsilon^0$)
Case I 1 and 2 or 3 and 4	$\begin{pmatrix}0 & 2\varepsilon_{12} & \\ 2\varepsilon_{12} & 0 & \\ & & 0\end{pmatrix}$	$(100)_R$ $((100)_{M2})$, $(010)_R$ $((001)_{M2})$	$2\varepsilon_{12}$ (0.0329)
Case II 1 and 3 Or 2 and 4	$\begin{pmatrix}\varepsilon_{11}-\varepsilon_{22} & & \\ & \varepsilon_{22}-\varepsilon_{11} & \\ & & 0\end{pmatrix}$	$(1\bar{1}0)_R$ $((20\bar{1})_{M2})$, $(110)_R$ $((201)_{M2})$	$\varepsilon_{11}-\varepsilon_{22}$ (3.29×10^{-5})
Case III 1 and 4	$\begin{pmatrix}\varepsilon_{11}-\varepsilon_{22} & 2\varepsilon_{12} & \\ 2\varepsilon_{12} & \varepsilon_{22}-\varepsilon_{11} & \\ & & 0\end{pmatrix}$	$(\sqrt{\frac{\varepsilon_{12}}{\varepsilon^0}+\frac{1}{2}},-\sqrt{-\frac{\varepsilon_{12}}{\varepsilon^0}+\frac{1}{2}},0)_R$ $((100)_{M2})$, $(\sqrt{-\frac{\varepsilon_{12}}{\varepsilon^0}+\frac{1}{2}},\sqrt{\frac{\varepsilon_{12}}{\varepsilon^0}+\frac{1}{2}},0)_R$ $((001)_{M2})$	$\sqrt{4\varepsilon_{12}^2+(\varepsilon_{22}-\varepsilon_{11})^2}$ (0.0329)
Case IV 2 and 3	$\begin{pmatrix}\varepsilon_{11}-\varepsilon_{22} & -2\varepsilon_{12} & \\ -2\varepsilon_{12} & \varepsilon_{22}-\varepsilon_{11} & \\ & & 0\end{pmatrix}$	$(\sqrt{\frac{\varepsilon_{12}}{\varepsilon^0}+\frac{1}{2}},\sqrt{-\frac{\varepsilon_{12}}{\varepsilon^0}+\frac{1}{2}},0)_R$ $((100)_{M2})$, $(\sqrt{-\frac{\varepsilon_{12}}{\varepsilon^0}+\frac{1}{2}},-\sqrt{\frac{\varepsilon_{12}}{\varepsilon^0}+\frac{1}{2}},0)_R$ $((00\bar{1})_{M2})$	$\sqrt{4\varepsilon_{12}^2+(\varepsilon_{22}-\varepsilon_{11})^2}$ (0.0329)

The stress-free transformation strain for the R to M1 transition is listed below,

$$\varepsilon_1=\begin{pmatrix}\varepsilon_{11} & 0 & \varepsilon_{23}\\ 0 & \varepsilon_{22} & 0\\ \varepsilon_{23} & 0 & \varepsilon_{33}\end{pmatrix},\varepsilon_2=\begin{pmatrix}\varepsilon_{11} & 0 & -\varepsilon_{23}\\ 0 & \varepsilon_{22} & 0\\ -\varepsilon_{23} & 0 & \varepsilon_{33}\end{pmatrix},\varepsilon_3=\begin{pmatrix}\varepsilon_{22} & 0 & 0\\ 0 & \varepsilon_{11} & \varepsilon_{23}\\ 0 & \varepsilon_{23} & \varepsilon_{33}\end{pmatrix},\varepsilon_4=\begin{pmatrix}\varepsilon_{22} & 0 & 0\\ 0 & \varepsilon_{11} & -\varepsilon_{23}\\ 0 & -\varepsilon_{23} & \varepsilon_{33}\end{pmatrix},$$

where $\varepsilon_{11}=-0.00219539, \varepsilon_{22}=-0.00386199, \varepsilon_{33}=0.00884465, \varepsilon_{23}=0.00412203$. The magnitude of the strain tensors is much smaller than that of M2 phase. Therefore, the applied stress or strain has a much greater influence on the stability of M2 than M1.

Structure relationship of R, M1 and M2 phases

Ignoring the non-tetragonality angle distortion, the unit vectors of M1 and M2 can be transformed from the R structure according to

$$\begin{pmatrix}\vec{a}_{M1}\\ \vec{b}_{M1}\\ \vec{c}_{M1}\end{pmatrix}\approx\begin{pmatrix}2\vec{c}_R\\ \vec{a}_R\\ \vec{b}_R-\vec{c}_R\end{pmatrix}, \text{ and } \begin{pmatrix}\vec{a}_{M2}\\ \vec{b}_{M2}\\ \vec{c}_{M2}\end{pmatrix}\approx\begin{pmatrix}2\vec{a}_R\\ 2\vec{c}_R\\ -\vec{b}_R\end{pmatrix}.$$

Table S2 Lattice parameters of the R, M1, and M2 structures [2,3].

Phase	Symmetry	Lattice constants (Å)			Angle (degree)
R, rutile	$P4_2/mnm$, (D_{4h}^{14})	a_R=4.55	b_R=4.55	c_R=2.85	90, 90, 90
M1, monoclinic	$P2_1/c$, (C_{2h}^{5})	a_{M1}=5.75	b_{M1}=4.54	c_{M1}=5.38	90, 122.6, 90
M2, monoclinic	C2/m, (C_{2h}^{3})	a_{M2}=9.07	b_{M2}=5.80	c_{M2}=4.53	90, 91.9, 90

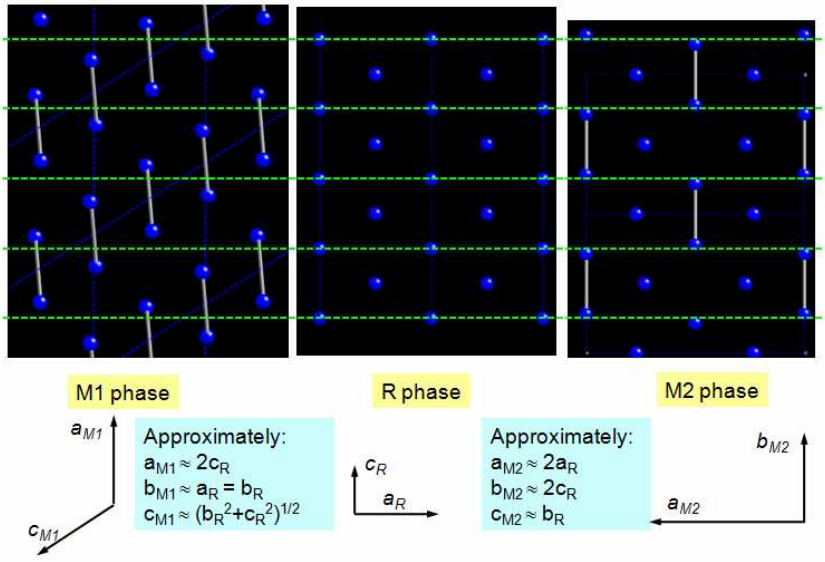

Figure S1 Side-viewed M1, R, and M2 structures of VO_2 (only vanadium atoms were shown). Left, M1 structure viewed along b_{M1} direction, showing dimerization of vanadium atoms and tilt of the pairs along a_{M1} (c_R) direction. **Middle**, R structure viewed along b_R direction. **Right**, M2 structure viewed along c_{M2} direction, showing half of the vanadium atoms dimerizing and the other half forming zigzag chains along b_{M2} (c_R) direction. Dashed lines are guides to the eye with respect to the unit cells along a_R direction.

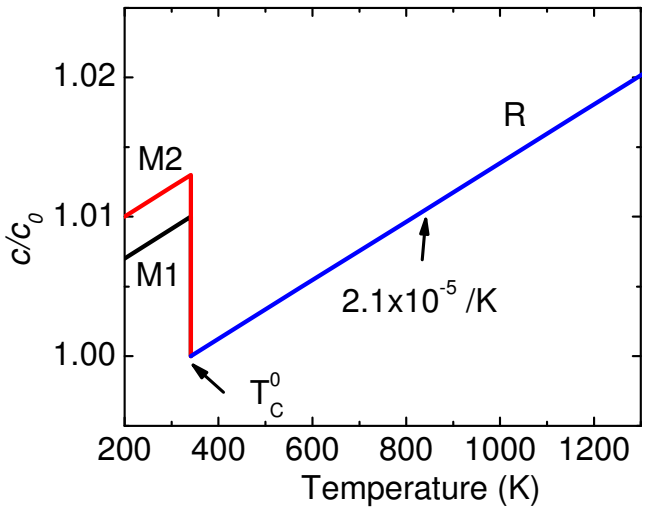

Figure S2 Natural effective lattice constant (c) of VO_2 along c_R direction as a function of temperature. The thermal expansion coefficient is assumed to be constant over the temperature range. c_0 is defined as the lattice constant in the R-phase near T_C^0. The abrupt jump in c/c_0 at T_C^0 is ~1% from R to M1 and 1.3% from R to M2. The thermal expansion of the SiO_2 surface is negligible on this scale. VO_2 beams were grown at temperatures ~1200 K. During the cooling process, the VO_2 microbeams can be frozen on the SiO_2 surface at different axial strain states, depending on local conditions during the cooling.

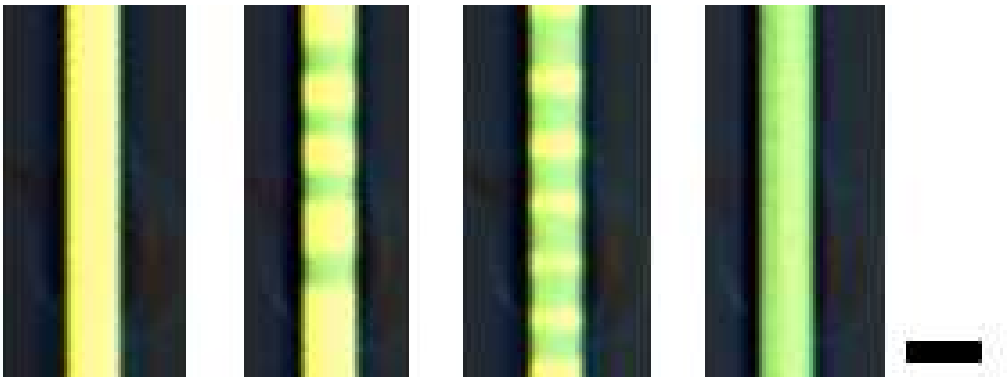

Figure S3 Bright-field reflected optical images of a bottom-clamped VO_2 beam under white light illumination. The temperatures are 298, 323, 333 and 368 K from left to right. The beams are in pure insulating phase (bright reflection) at 298 K and pure metallic phase (dark reflection) at 368 K, and mixed insulating-metallic domains at intermediate temperatures (323 and 333 K). The scale bar is 2 μm.

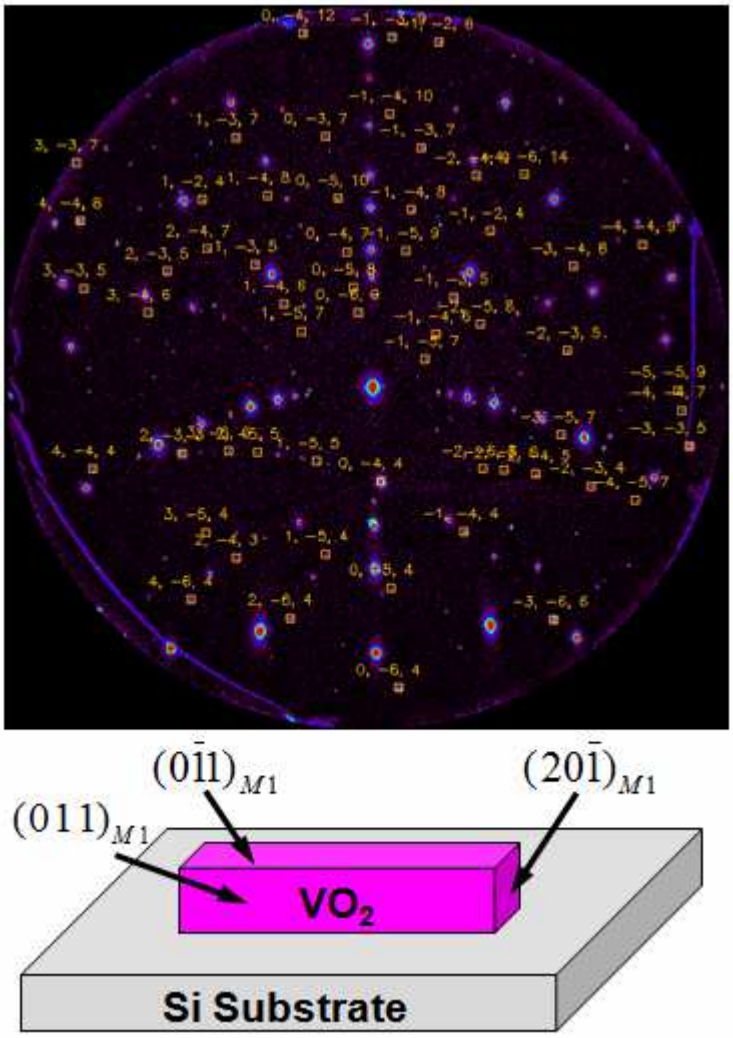

Figure S4 Laue diffraction pattern of a free-standing VO_2 microbeam at room temperature indexed to the M1 phase. The brightest spots are from the Si substrate. The rest of spots can be indexed as the M1 phase. The bottom is a schematic view of the VO_2 beam with bounding surfaces labeled.

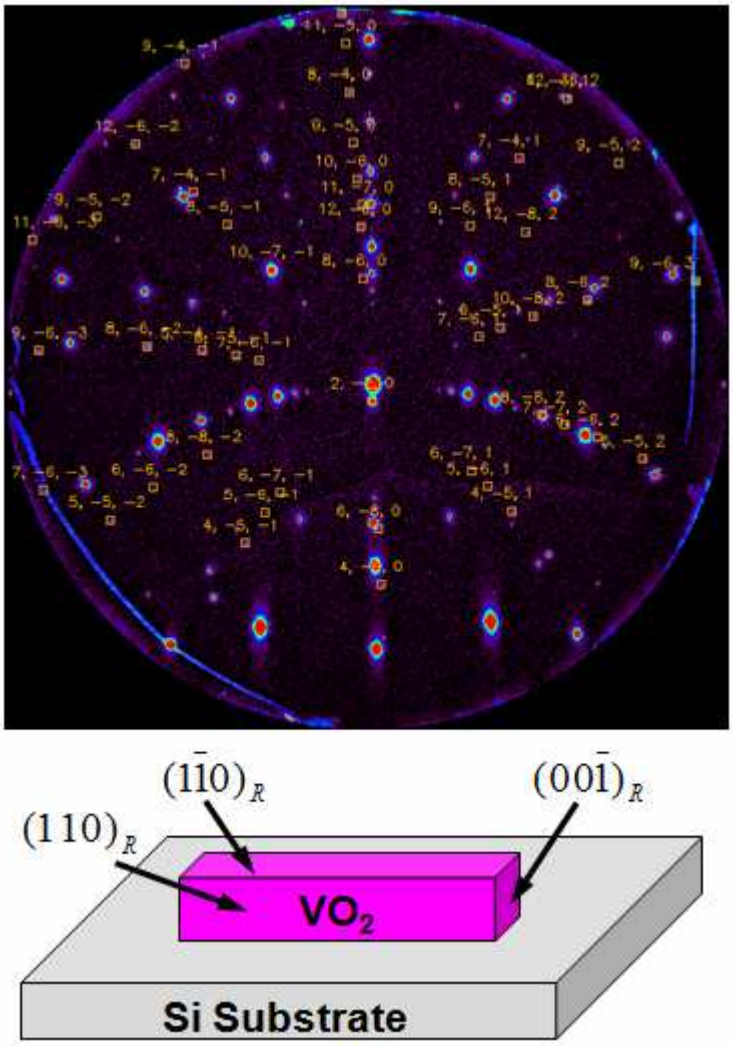

Figure S5 Laue diffraction pattern of the free-standing VO_2 microbeam at 360 K indexed to the R phase.

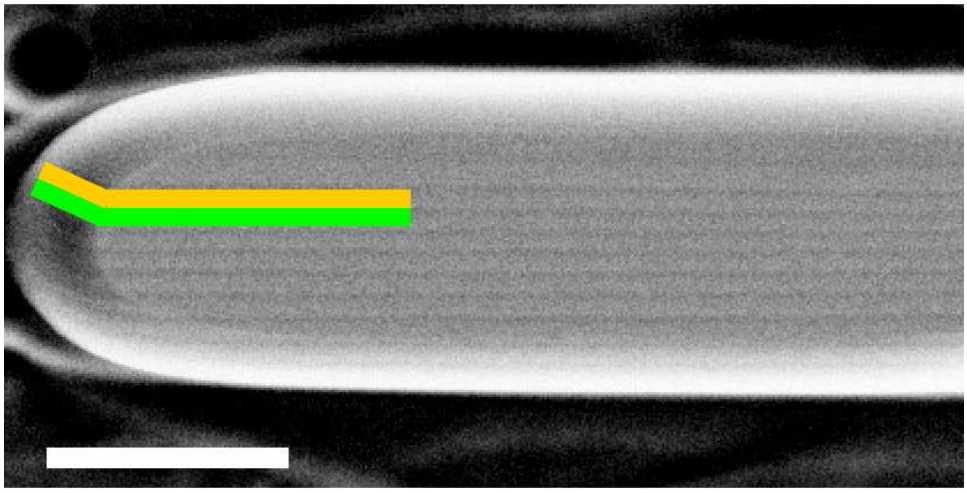

Figure S6 Kinks of M2 stripes at the edge of a bottom-clamped VO_2 beam. Top-viewed high-resolution SEM image of a bottom-clamped VO_2 beam with a round end showing apparent kinks at the edge, indicating that the twined platelets (M2α and M2β domains) tilt with respect to the direction perpendicular to the substrate. The temperature is 323 K. The colored lines are guide to the eyes. The scale bar is 1 μm.

References

[1] Khachaturian, A.G., *Theory of structural transformations in solids*. (John Wiley & Sons New York, 1983).

[2] Eyert, V., The metal-insulator transitions of VO_2: a band theoretical approach. *Ann. Phys.-Berlin* **11**, 650-702 (2002).

[3] Marezio, M., McWhan, B., Dernier, P.D., & Remeika, J.P., Structural Aspects of Metal-Insulator Transitions in Cr-Doped VO_2. *Phys. Rev. B* **5**, 2541 (1972).